Experimental investigation, modeling, and simulations for MEMS based gas sensor used for monitoring process chambers in semiconductor manufacturing

Ijaz H. Jafri[a]♦, Frank DiMeo Jr. [b], Jeffrey Neuner[b], Sue DiMascio [b], and James Marchetti[a]

[a]IntelliSense Corporation, 36 Jonspin Road, Wilmington, MA 01887
[b]Advanced Technology Materials, Inc., 7 Commerce Drive, Danbury, CT 06810

ABSTRACT

There is a growing demand from the semiconductor industry for multi-component gas sensing for advanced process control applications. Microelectromechanical systems (MEMS) based integrated gas sensors present several advantages for this application such as ease of array fabrication, small size, and unique thermal manipulation capabilities. MEMS based gas sensors that are produced using a standard CMOS (Complimentary Metal Oxide Semiconductor) process have the additional advantages of being readily realized by commercial foundries and amenable to the inclusion of on-chip electronics.

In order to speed the design and optimization of such integrated gas sensors, a commercial software package IntelliSuite[TM] was used to model the coupled thermo-electro-mechanical responses of devices known as microhotplates. Models were built based on the GDSII formatted mask layout, process sequences, and layer thicknesses. During these simulations, key parameters such as device design and structure were investigated, as well as their effect on the resultant device temperature distribution and mechanical deflection. Detailed analyses were conducted to study the resonance modes for different sensor configurations, such as fixed-end and springboard arrangements. These analyses also included a study of the effect of absorbed material on device natural frequency.

The modeling results from this study predict that the first three resonant frequency modes for these devices are in the 612 to 1530 kHz range for an all pinned device, and 134 to 676 kHz for a springboard arrangement. Furthermore, the modeling suggests that the resonant frequencies will decrease linearly as a function of increasing absorbed mass, as expected for a simple spring model. The change in resonant frequency due to mass absorption is higher for an all-pinned arrangement, compared to a springboard arrangement, with the second and third (twisting mode) showing the largest change. Thermo-electro-mechanical simulations were also performed for these devices, and the predicted mechanical deformations resulting from applied voltage compare favorably with experimental observations.

Keywords: CMOS based gas sensors, MEMS, modeling and simulation, process monitoring, coupled analysis, micromachining, microhotplate.

1. INTRODUCTION

The semiconductor industry is moving inexorably towards sensor driven processing as more stringent environmental concerns arise, and as increasing wafer sizes make processing mistakes prohibitively expensive [1]. *In situ* and on-line process control offers significant efficiency and cost benefits, but because a suitable detection system does not yet exist, the microelectronics industry has not embraced this approach. Solid-state gas sensors have been used by the semiconductor industry for both life safety and process applications [2], and examples of such gas sensors include devices that detect unsafe levels of poisonous and/or explosive gases in breathing-space environments, and devices that continuously monitor humidity and contaminant levels within process gas streams. However, significant issues with existing technologies limit their further use for *in situ* semiconductor process control. These limits include poor stability, slow response times, and most importantly interference effects from constituents other than the target gases [3].

Solid-state sensors rely on the occurrence of chemical interaction between the probed environment and the active portion of the sensor to produce a signal that can be interpreted to provide species concentrations. A limited level of selectivity can be introduced by altering the type of active material employed as reported by Morrison [4], but it has been recognized that

♦ Correspondence: I. H. Jafri. Email: IJafri@intellisense.com; Telephone: +1(978)988-8000; Fax: +1(978)988-8001

temperature changes can greatly affect the functionality of the solid-state devices by changing interaction kinetics and other properties [5]. In addition, it has also been recognized that increasing the number of sensing elements is another means of providing flexibility and improving selectivity.

It is a natural extension to combine the use of temperature with the use of multiple elements to achieve improved selectivity, and this approach has been taken by a number of groups. Advances in thin film processing, and more recently micromachining techniques, have made this an extremely attractive approach. For example, Ikegami et al. [6] fabricated a uniformly heated array of six elements on an alumina substrate, and used this array to identify gases such as ammonia, methanol, and hydrogen sulfide. Chang et al. [7] have described an integrated sensor with an individual heater element fabricated using silicon integrated circuit thin film techniques. However, these sensor elements were not thermally isolated from the substrate, and therefore were limited in the maximum temperature that could be achieved and did not exhibit fast thermal response times.

Using micromachining techniques, Wang et al. [8] constructed an array of sensor elements fabricated on silicon membranes, which provided improved thermal isolation of the active area. In this device, there was a separate temperature sensing layer or integrated heater to heat the sensing layer of materials grown above it. Najafi et al. [9] describe an integrated multi-element gas sensor created by micromachining techniques that uses an integrated heater, silicon resistor temperature sensors, and sensing film with four contacts. The temperature measurement was done using resistors, which were inter-digitated with the heaters. In both of these approaches, custom fabrication techniques were used, potentially increasing the cost of commercialization.

The use of commercially available integrated circuit fabrication technology, i.e. standard CMOS processes, is a significant advantage because it is readily available through production foundries, typically has a high yield, and is amenable to the integration of on-board analog and digital circuitry. Using standard CMOS foundry processes and some post processing, a variety of devices have been demonstrated such as resistive heaters [10], resistive temperature sensors [11], thermal actuators [12], and thermoelectric sensors [13]. Conductometric gas sensors have also been designed and fabricated by several groups [14]. The devices consist of material layers that are used in standard CMOS process, such as polysilicon and aluminum encapsulated by silicon oxide. The subsequent micromachining of the underlying silicon releases these surface layers, forming membranes with high thermal isolation and thus with unique thermo-electro-mechanical properties.

In order to expedite the design and optimization of such integrated gas sensors, a commercial software package IntelliSuite[TM] was used to model the coupled thermo-electro-mechanical responses of devices known as microhotplates. Three-dimensional models were built based on the mask layout, process sequences, and layer thicknesses. Details of the device, modeling procedure, modeling results, and comparison with experiments will be discussed in the following sections.

Figure 1: Device layers

2. MICROHOTPLATE GAS SENSOR DESCRIPTION

ATMI, in collaboration with IntelliSense Corporation, is currently developing a multi-component gas sensing system for semiconductor fabrication process control. The heart of the system is based on the MEMS device structure known as the microhotplate, which is produced through a combination of standard CMOS technology and MEMS post-processing as described in the literature [15,16,17,18,19,20,21]. Figure 1 shows a schematic of an individual microhotplate structure, which consists of a thermally isolated, suspended resistive heater, a thin film thermometer, and four contact pads for measuring the conductance of the active layer. Figure 2 shows an optical micrograph of a 4-element array. The most noticeable physical characteristics of these devices are their extremely fast thermal rise (1-3 msec) and fall times (3-4 ms), which enable the measurement of transient responses. Other important physical characteristics include the small suspended mass (about 0.2 µg), small area (100µm x 100µm), low power consumption (<60
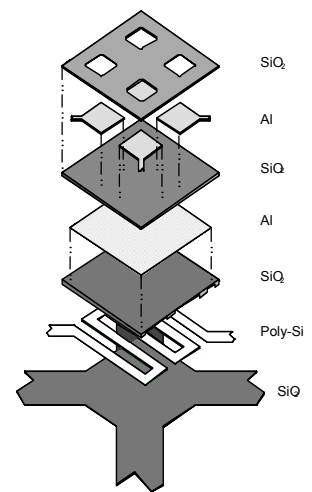
200 microns
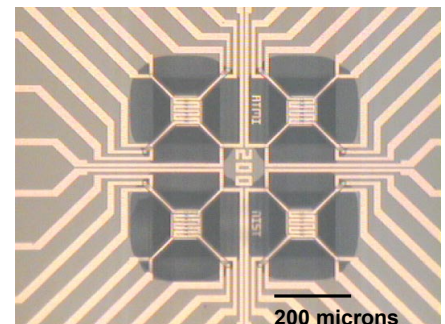
Figure 2: Array of 4x4 gas sensor

mW) and high maximum surface temperature (500°C). The microhotplate gas sensors modeled and used in this study were produced using the MOSIS fabrication service [22]. The as-received dies were etched to release the thermal isolation layers using gas phase silicon isotropic etchant (XeF$_2$) as described in literature [23, 24].

Typically, this structure has been used as a conductometric sensor, where the change in conductance of the sensing layer is a measure of the gases present. However, the suspended device can also be used as a micro oscillator, where changes in resonant frequency are indicative of absorbed mass. Berger et al. [25] have calculated that the minimum detectable mass changes can be on the order of 10^{-12} grams, for a similar but simplified cantilever structure with a structural mass on the order of $\sim 10^{-9} - 10^{-6}$ grams.

The actual microhotplate structures in this study are significantly complex, with variable density material in different layers and variable geometries within a layer. A detailed finite element analysis is needed to predict the vibrational behavior of these devices, as well as the coupled thermo-electro-mechanical response and properties. A parametric study that can identify those designs with the highest frequency change for a given absorbed mass or identify areas of high thermo-mechanical stress can help greatly in design optimization. Such a finite element analysis (FEA) was conducted for the several microhotplate designs using IntelliSuite^{TM}. This analysis consisted of the creation of the 3D finite element mesh, verification of the consistency of the model mesh size, and subsequent parameter extraction, such as resonant frequency behavior as a function of mass load, and mechanical deformation due to thermal expansion. These results, as well as a comparison to measured device behavior will now be presented.

3. FEA MODEL CREATION

A microhotplate device model was created using the process simulator and GDSII mask converter in IntelliSuite^{TM}. Table 1 shows the thin film and bulk material property data used in modeling and numerical simulations. Estimated thicknesses were used for mesh optimization studies. Based on this information, a solid model was created (shown in Figure 3). The model was then meshed using 20-node brick elements and transferred for analysis. For finite element analysis, the device legs were truncated at the corners and a fixed (zero displacement) boundary condition was used at the attachment points. Figure 4 shows the device solid model (meshed) for FEA analysis.

For finite element analysis, mesh size has a significant effect on the results. Before starting detailed coupled thermo-electro-mechanical analyses, a mesh refinement and optimization study was conducted to investigate the effect of mesh size. The actual device design consists of complex multi-layer structures, such as a serpentine heater layer and other non-symmetric features, which make the structure numerically complicated to model. Since a symmetric boundary condition cannot be used due to the geometry, the model space / size is difficult to reduce. The steepest
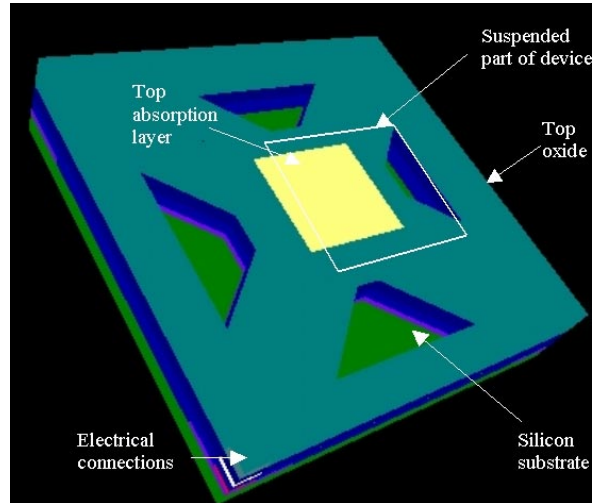
Figure 3: Three-dimensional solid model
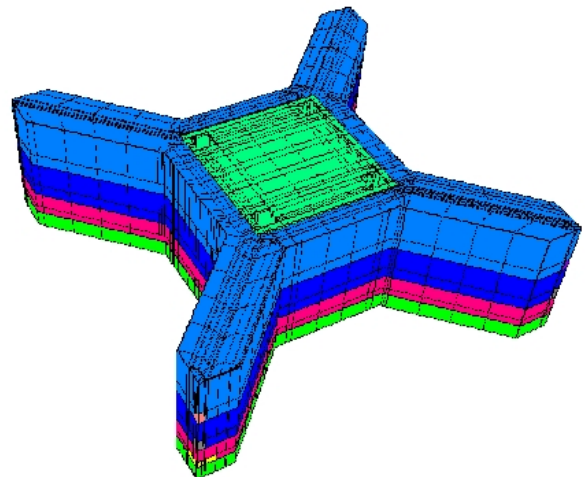
Figure 4: Meshed solid model for FEA analysis (shown 10x in z dimension)
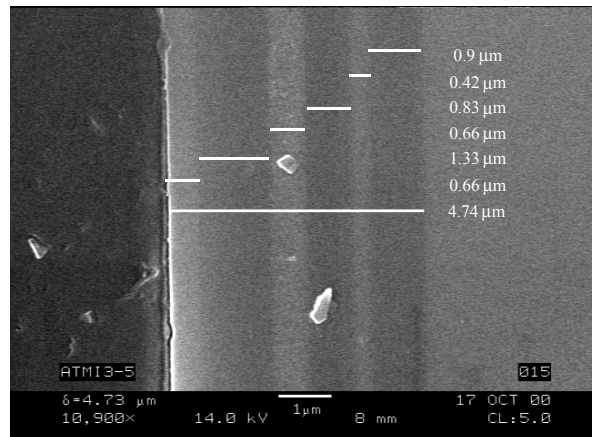
Figure 5: Device thicknesses under SEM

deflection gradients occur in device legs, hence for this investigation, the complex features in the middle of the device were replaced with the oxide layer mask and model was created from single mask (silicon oxide). This simplification reduced the model significantly, and had no major affect on the results, as the automatic mesh refinement in the center of the device does not play a significant role in mesh studies. Therefore, the mesh was only refined locally in the device legs section. Several mesh sizes were investigated with the goal of finding the smallest number of nodes that produce consistent results.

Table 1: Thin film and bulk material properties used for simulation				
Property	**Units**	**Polysilicon**	**SiO$_2$**	**Aluminum**
Stress	M Pa	0	0	0
Density	gm/cc	2.3	2.2	2.7
Coefficient of Thermal Expansion	10^{-7}/C	20	5.2	250
Resistivity	ohm.cm	3.22×10^{-5}	1.00×10^{9}	4.80×10^{-5}
Thermal Conductivity	W/cm.C	0.6	0.014	2.36
Specific Heat	J/g.C	0.678	0.8	0.9614
Young's Modulus	G Pa	160	73	68.85
Poisson's Ratio		0.226	0.175	0.36
Dielectric Constant		4.2	3.9	1

Table 2: Mesh refinement – Multilayer oxide model			
# of nodes	**Max. Mesh size Microns**	**Frequency (First mode) Hz**	**Change %**
1377	84	475,136	-
5306	20	363,332	30.8
17039	10	353,994	2.6

Table 2 shows the effect of grid size on natural frequency values. These results indicate that as the mesh size is decreased, initially there is a significant improvement in results accuracy. However, the change in frequency value reduces significantly upon further refinement. When the grid size is reduced from 84 microns to 20 microns (which corresponds to about 285% increase in the number of nodes in the model), the results change about 31%. As the grid size is reduced to 10 microns (which corresponds to about 1137% increase in number of nodes compared to 84 microns mesh size), the impact on results is minimal - with less than 3% change (from 20 microns mesh size model). This indicates that grid independence has been reached. This baseline mesh size (20 microns) will be used in the analyses discussed below.

Table 3: Measured thicknesses		
Layer	**Material**	**Measured Thickness (μm)**
1	Field Oxide	0.90
2	Polysilicon	0.42
3	Oxide	0.83
4	Metal 1	0.66
5	Oxide	1.33
6	Metal 2	0.66
7	Overglass	2.0

4. EFFECT OF MASS ON DEVICE RESONANT FREQUENCY

An SEM was taken of the cross-section of the device (Figure 5) to measure the various layer thicknesses of the microhotplate. The experimentally measured thicknesses are listed in Table 3. After establishing the optimum grid size and exact layer thicknesses, resonant frequencies for the device were obtained using FEA methods. This analysis predicts that that the first three modes of the resonant frequency of the device will be approximately 612, 1522, and 1530 kHz, respectively, for all four post arrangements, and 134, 382, and 676 kHz for a springboard or two post arrangement.

After obtaining the resonant frequencies of the baseline device, the effect of mass on the resonant frequency was obtained next. A simple prediction of the resonant frequency of a structure is given by:

$$f_n = \frac{1}{2\pi}\sqrt{\frac{k}{m}} \tag{1}$$

This model will not be accurate for rotational modes. If more material is added to the structure without changing its material properties or stiffness, the new frequency of the structure can be obtained from:

$$f_{new} = f_{old}\sqrt{\frac{m_{old}}{m_{new}}} \tag{2}$$
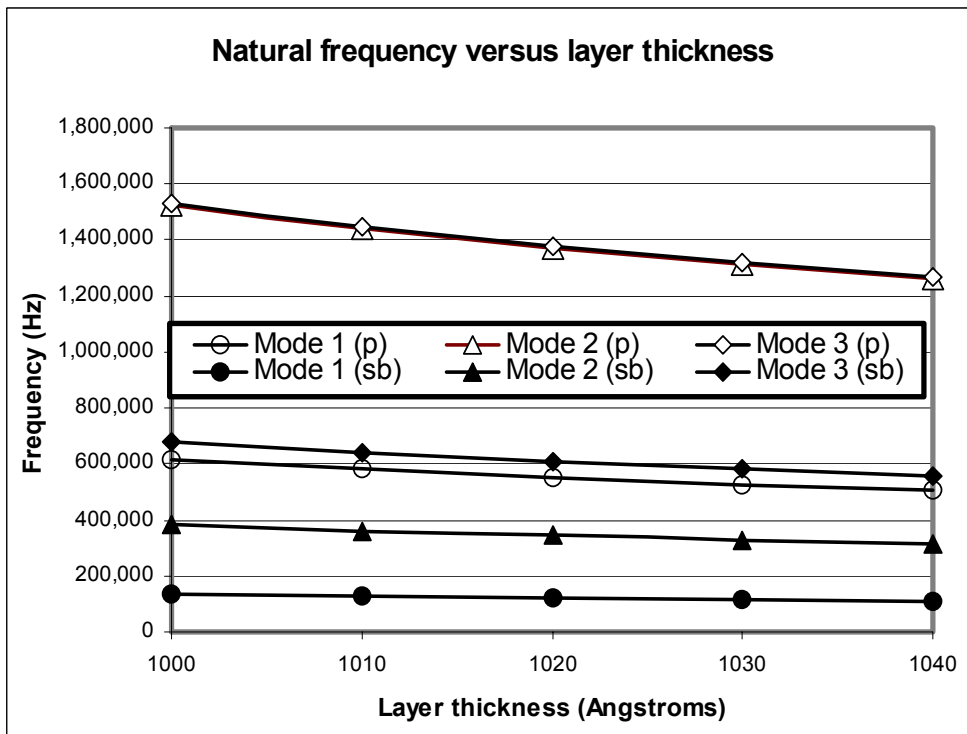
Figure 6: Resonant Frequency versus layer thickness

To test the applicability of this simple model, new resonant frequencies were calculated as a function of absorbed mass, assuming no change in material density of the structure. It was also assumed that the material is uniformly absorbed, resulting in formation of a layer of uniform thickness, on the order of a few mono-layers (~10 Angstroms). Increments of approximately 11 nanograms of material were added. These analyses (see Table 4) indicate that the change in frequency is higher for the four legged arrangement compared to the springboard arrangement for same amount of absorbed mass. Also the second and third modes (twisting modes) of frequency seem to be very close to each other in both the two and four post structures. The second and third mode of the four-post arrangement has the highest change in frequency value for the same amount of absorbed mass (Figure 6). Hence, it may be beneficial to monitor these two modes to detect the changes in mass

rather than the first mode. These analyses are quite useful for device design in that they identify the range of resonant frequencies and help in optimizing device performance. Furthermore, the four post design has a higher resonant frequency and may be advantageous because it will provide higher incremental change values for an equal change in mass.

5. EXPERIMENTAL AND NUMERICAL THERMO-ELECTRO-MECHANICAL ANALYSES

The coupled thermo-electro-mechanical analysis was the next modeling task performed, and was also done using the IntelliSuite^{TM} software package. The first aspect investigated was the thermal distribution of the microhotplate surface that occurs as a result of applying power to the polysilicon heater. The FEA model in IntelliSuite included the top active layer. A temperature independent electrical resistivity of 1.26×10^{-5} Ω.m (that corresponds to about 2400 Ω) was used for the serpentine polysilicon heater. Steady state three-dimensional Joule heating and conduction modeling was performed with no convection or radiation losses used in the model. For these simulation studies, thermal conductivity was also assumed to be constant, and voltage was varied allowing the reactive current to float and adjust according to the material properties and device dimensions. The choice of thermal boundary conditions has a significant affect on device modeling. In the present numerical analysis, the attachment of the posts of upper and lower oxide layers of the device were held at a constant temperature of 50°C. This is reasonable, as the substrate will act as a considerable heat sink at these areas. The temperature on all other layers was allowed to float and adjust according to the applied power.

Figure 7 shows the temperature distribution for an applied power of 6.667 mW for the top silicon oxide, embedded polysilicon heater, aluminum metal layer and top active layer. This analysis indicates that there is surface uniformity of approximately 4°C across the top active layer portion of the device. Figure 8 shows the device temperature variation in various layers as a function of applied power, indicative of the thermal distribution perpendicular to the surface. Under steady state conditions, the temperature gradient in the device from one layer to the next is very small. As the power increases, the temperature gradient

Temperature Dist.   deg_C
124.118
117.38
110.642
103.904
97.166
90.428
83.69
76.952
70.214
63.476
56.738
50

Temperature Dist.   deg
124.757
117.961
111.165
104.369
97.5726
90.7765
83.9805
77.1844
70.3883
63.5922
56.7961
50

Temperature Dist.   deg
124.174
117.949
111.723
105.498
99.2729
93.0476
86.8224
80.5971
74.3718
68.1465
61.9213
55.696

Temperature Dist.   deg_C
124.034
123.523
123.012
122.501
121.99
121.479
120.968
120.457
119.946
119.435
118.924
118.413

Figure 7: Temperature distribution at various device layers. Absorption layer magnified 25x for clarity

from one layer to the next increases slightly, but is not appreciable. The temperature variation is about 1 degree layer to layer at low power and about 5 degrees at higher power. In the model, the primary heat flow is via conduction through the device legs. In an actual device, there may be appreciable heat losses via convection and radiation at higher power, which is expected to increase the temperature gradient across the device layers (perpendicular). Thus the temperature variation from one layer to the next layer as predicted by the model may be lower than the experimental observations. This variation will be higher at elevated temperatures.

| | | Table 4: Resonant Frequency | | | | | |
| | | Pinned | | | Springboard | | |
Top layer thickness (A^0)	Device Mass (kg)	Mode 1 (p)	Mode 2 (p)	Mode 3 (p)	Mode 1 (sb)	Mode 2 (sb)	Mode 3 (sb)
1000	9.6960E-11	612,315	1,522,320	1,530,260	134,225	382,098	676,838
1010	1.0808E-10	579,961	1,441,883	1,449,404	127,133	361,909	641,075
1020	1.1920E-10	552,248	1,372,983	1,380,144	121,058	344,615	610,441
1030	1.3032E-10	528,162	1,313,101	1,319,950	115,778	329,585	583,817
1040	1.4144E-10	506,975	1,260,427	1,267,001	111,134	316,364	560,398
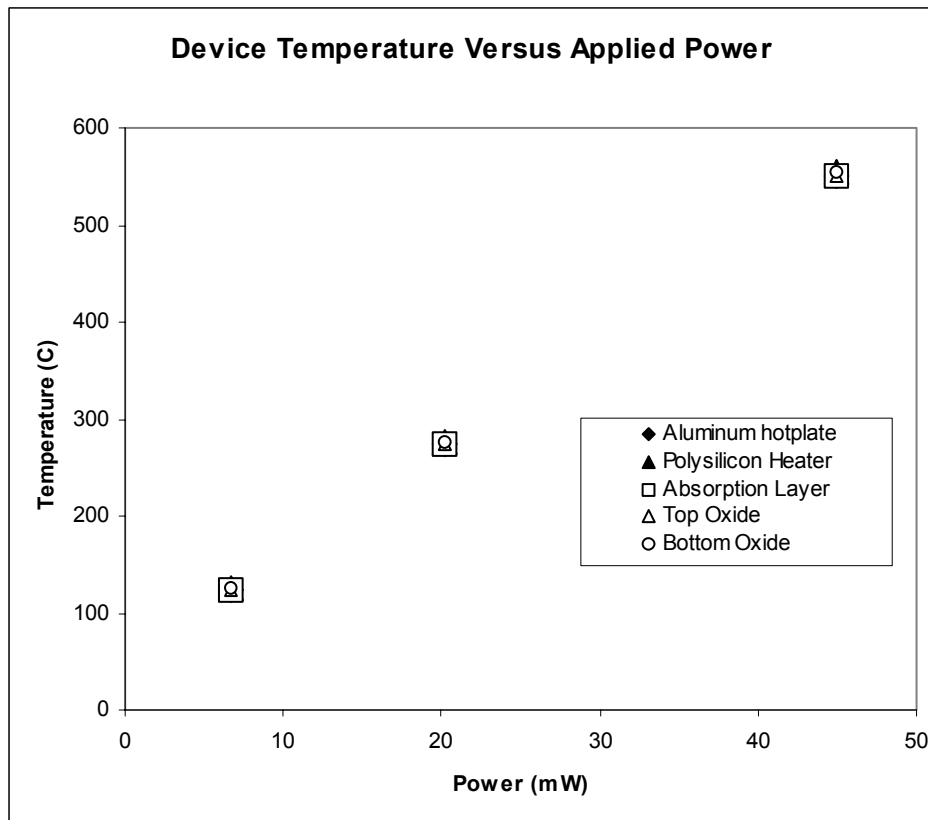
Figure 8: Device temperature versus power

In conjunction with producing thermal gradients, applying power to the device results in mechanical deformation due to thermal expansion of the device structure. Figure 9 shows the deformation of the device under voltage load based on numerical simulations. Notice that the device is bowed towards the etch pit. A series of simulations were done, and data for device deflection as a function of applied power were obtained and compared with experimental observation (Figure 10).

For the experimental observation of device deflection as a function of applied power, a Digital Instruments Atomic Force Microscope (AFM) was used. An unpackaged, uncoated sample was mounted and held in place on the AFM stage using double-sided tape. Two mechanical probes were used to power the polysilicon heater through the contact pads. A Keithley 224 programmable current source provided the input current and the voltage was monitored using a fluke digital micrometer (DMM). The sample device was brought into focus on the AFM with no power applied and the AFM in tapping mode. The current was applied at three different settings in order to observe the displacement for each power level.   In all cases, microhotplate moved down towards the etch pit, as predicted by the modeling.

The results shown for device deflection as a function of applied power (Figure 10) show an excellent agreement at low power level. However, as the power level is increased, the deflection predicted by the model is lower than what is experimentally observed. These first order modeling analysis results are very encouraging. The deviations between the model and experiment at high temperature point out important areas that may need further refinements and modeling improvements.

Device deflections shown via simulations as well as measured by experiments are within the 40% of each other at the highest power simulated and measured, which is quite reasonable given the assumptions that were made in the model. These assumptions include:

1) The use of temperature independent electrical and thermal conductivity, particularly in the polysilicon layer.
2) The modeling of only conductive heat loss, with no convective or radiative component.
3) The use of bulk material property data when thin film data was not available for a specific material.
4) The lack of incorporation of possible pre-existing stresses in the as deposited layers.
5) The use of a constant temperature boundary condition at the device attachment points
6) The device was perfectly etched and fully released.

Displacement Z	µm
	0.00185107
	−0.0102165
	−0.022284
	−0.0343516
	−0.0464191
	−0.0584867
	−0.0705542
	−0.0826218
	−0.0946893
	−0.106757
	−0.118824
	−0.130892
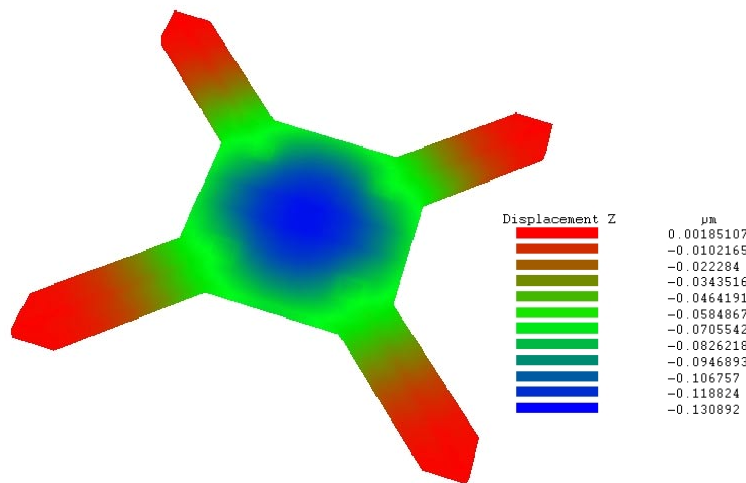
Figure 9: Device deflection at 6.667 mW

It should also be noted that the experimental device did not have the top active layer, which had been simulated during the modeling analysis. Also, a steady state non-transient response was modeled for the device. From the observation that the difference between the model and experiment increase with increasing temperature, it is likely that the first of the listed assumptions is dominant. The lack of other a temperature dependent resistivity in the heater may result in a modeled temperature lower than that actually achieved, which would result in a lower deflection. The other assumptions should be verified, however. For example, the effect of stresses during fabrication and etching processes can have a significant effect. This stress can either add to the thermal stress (and strain - if it is compressive) or react opposite to the thermal stress (and

strain – if it is tensile) during device heating. It may be possible that some of the assumptions are actually offsetting, i.e. we have underestimated the effect of stress, but over estimated the material bulk values. Additionally, it should be noted that the electrical resistivity of device as reported by the manufacturer varies 5 –10 % from batch to batch. Typical room temperature sheet resistivity is in the range of about 30 to 32.4 ohms/square, corresponding to about 1.26×10^{-5} to 1.36×10^{-5} Ω.m (for a 0.42 micron thick layer of doped polysilicon). Wherever possible, measured materials properties should be incorporated in the model for the most accurate comparisons. Further work is underway to evaluate these and the other sources of possible variations such as incorporating temperature dependant convective and radiative heat transfer as well as material properties (thermal conductivity and electrical resistivity).   On the experimental side, more work is needed to get an absolute temperature measurement, ensure fully released structure and measure process induced stresses in device.
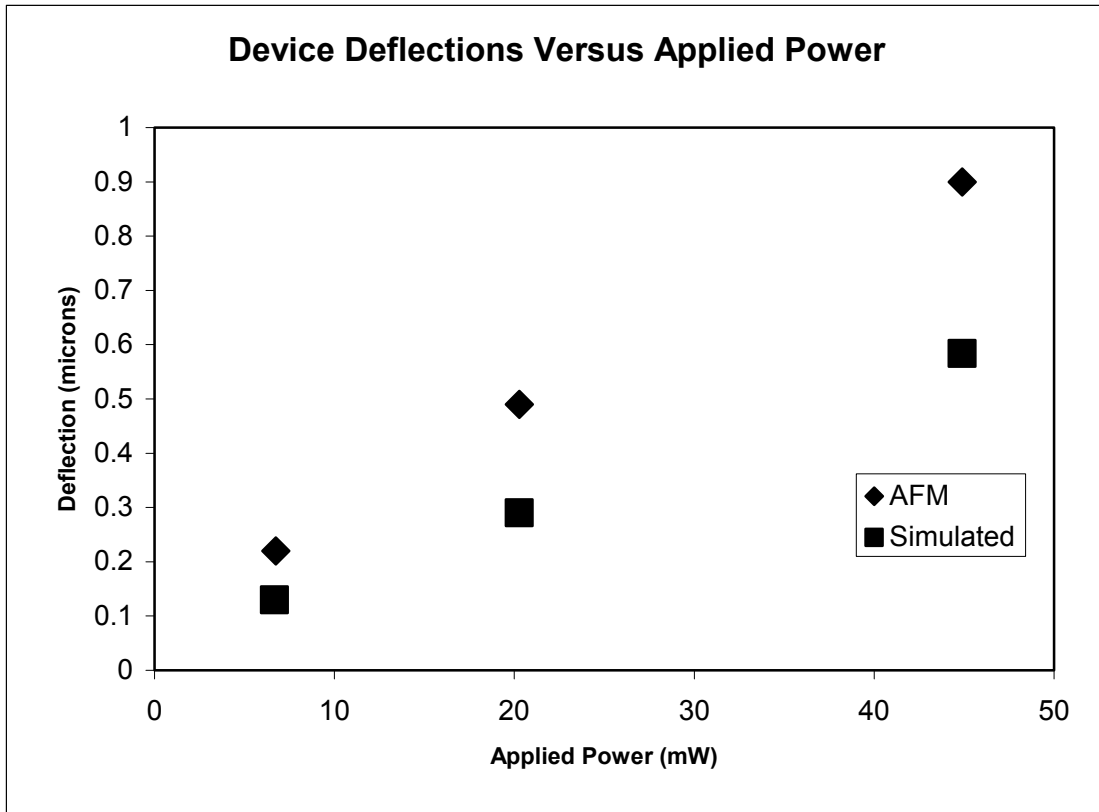
Figure 10: Device deflection (experimental and simulated)

6. CONCLUSIONS

In this work we have used finite element modeling to predict the coupled thermo-electro-mechanical properties of CMOS based microhotplates. We have used the measured thickness of the thin film layers as inputs to the model, and calculated the resonant frequency as a function of absorbed mass. The analyses predict that the first three modes of natural frequency are 612, 1522, and 1530 kHz for the four post device, and 134, 382, and 676 kHz for a two post, or springboard arrangement. The four post device has a higher change in resonant frequency with added mass, and the second and third mode have higher changes compared to the first mode. Atomic force microscopy was used to experimentally measure the mechanical deflection of the device as a function of power. The simulation results agree very well with the experimental data at low power. At higher power, however, the model and experimental results begin to diverge. We attribute this to the effect of convective and radiative loses and temperature dependent material properties, and are currently working on improving the model by incorporating these effects. The ability to accurately model the coupled thermo-electro-mechanical behavior is a significant accomplishment, and one that we expect will speed the design and optimization of a CMOS based integrated gas sensor.

ACKNOWLEDGEMENTS

REFERENCES

1. National Technology Roadmap for semiconductor technology needs, 1997 edition, pp 183

2. N. Yamazoe and T. Seiyama, *Proc. of 3rd International Conf. On Solid State Sensors and Actuators,* IEEE, Philadelphia, pp 376, 1985

3. P.T. Mosley and B.C. Tofield, *Solid State Gas Sensors,* Adam Hilger, Bristol, 1987

4. S.R. Morrison, *Proc. of the 2nd Int'l meeting on chemical sensors*, Bordeaux, pp. 39, 1986

5. J.F. McAleer, P.T. Moseley, J.O.W. Norris and D.E. Williams, *J. Chem. Soc. Faraday Trans. I*, 83, pp. 1323, 1987

6. A. Ikegami and M. Kaneyasu, 1985 Digest of Technical Papers, *Int. Conf. Solid State Sensors and Actuators, Transducers 85*, IEEE Library of congress 84-62799, pp. 74, 1985

7. S.C. Chang and D.B. Hicks, 1985 Digest of Technical papers*, Int. Conf. Solid State Sensors and actuators, Transducers 85*, IEEE Library of congress 84-62799, page 381

8. X. Wang, S. See and P. Carey, *Proc. Of the 1992 IEEE workshop on sensors* , Hilton Head, pp. 23, 1992

9. N. Najafi, K. D. Wise, R. Merchant and J.W. Schwank, Proc. Of the 1992 IEEE workshop on sensors , Hilton Head, p 19

10. M. Parameswaran, A.M. Robinson, D.L. Blackburn, M. Gaitan, and J. Geist, "Micromachined thermal radiation emitter from a commercial CMOS process", *IEEE Electron Device Lett.*, 12, no. 2, pp 57-59, Feb. 1991

11. M. Parameswaran, A.M. Robinson, L.J. Ristic, K. Chau, and W. Allegretto", A CMOS thermally isolated gas flow sensor", *Sensors and Materials*, 2, pp 17-26, 1990

12. D. Moser, O. Brand, H. Baltes, "A CMOS compatible thermally excited silicon oxide beam resonator with aluminum mirror", *Proc. Transducers*, pp. 547-550, 1991

13. J. Jaeggi, H. Baltes, and D. Moser, "Thermoelectric AC power sensor by CMOS technology", *IEEE Electron Device Lett.*, 13, no. 7, pp. 366, 1992

14. M. Parameswaran, H.P. Baltes, L.J. Ristic, A.C. Dhaded, and A.M. Robinson, "A new approach for the fabrication of micromachined structures", *Sensors and actuators*, 19, pp. 289-307, 1989

15. US Patent No, 5,356,756

16. US Patent No. 5,345,213

17. R. Cavicchi, J. Suehle, K. Kreider, M. Gaitan, "Fast temperature programmed sensing for microhotplate gas sensors", *IEEE Electron Devices Letters*, Vol. 16, No.6, pp.286-288, June 1995

18 S. Semancik, R. Cavicchi, K. Kredier, J. Suehle, P. Chaparala, "Selected area deposition of multiple active films for conductometric microsensor arrays", *Transducers 95 (Eurosensors IX),* pp 831-834, June 1995

19 R. Cavicchi, J. Suehle, K. Kreider, B. Shomaker, J. Small, M. Gaitan, "Growth of SnO_2 films on micromachined hotplates", *Appl. Phys. Lett.* Vol. 66, No. 7, 1995

20 F. Dimeo Jr., S. Semancik, R. Cavicchi, J. Suehle, N. Tea, M. Vaudin, J. Kelliher, "Silicon microhotplate arrays as a platform for efficient gas sensing thin film research*", Mater. Res. Soc. Symp. Proc.* Vol. 444, pp. 203, 1997

21. F. DiMeo, Jr., R. Cavicchi, S. Semancik, J. Suehle, N. Tea, J. Small, J. Armstron, J. Kelliher, "In situ conductivity characterization of oxide thin film growth phenomena", *J. Vac. Sci. Tech. A,* Vol. 16, No.1, pp. 131-138, 1998

22. http://www.mosis.org

23. P. Chu, J. Chen, R. Yeh, G. Lin, J. Huang, B. Warneke, and K. Pister "Controlled Pulse-etching with XeF2", *Transducers 97, the 9th Inter. Conf. Solid State Sensors and Actuators*, Chicago, IL, June 1997.

24. K. Williams and S. Muller, "Etch rates for micromachining processing", J. MEMS, 5, No. 4, pp. 256-269, 1996

25. R. Berger, *Microelectron Eng.*, 35, pp 373-379, 1997